

Title	Deep learning assisted robust detection techniques for a chipless RFID sensor tag
Authors	Rather, Nadeem;Simorangkir, Roy B. V. B.;Buckley, John L.;O'Flynn, Brendan;Tedesco, Salvatore
Publication date	2023-11-28
Original Citation	Rather, N., Simorangkir, R. B. V. B., Buckley, J. L., O'Flynn, B. and Tedesco, S. (2023) 'Deep learning assisted robust detection techniques for a chipless RFID sensor tag', IEEE Transactions on Instrumentation and Measurement, 73, 2502710 (10pp). doi: 10.1109/TIM.2023.3334378
Type of publication	Article (peer-reviewed)
Link to publisher's version	10.1109/tim.2023.3334378
Rights	© 2023, the Authors. This work is licensed under a Creative Commons Attribution 4.0 License. For more information, see https://creativecommons.org/licenses/by/4.0/ - https://creativecommons.org/licenses/by/4.0/
Download date	2025-06-07 02:07:45
Item downloaded from	https://hdl.handle.net/10468/15287



UCC

University College Cork, Ireland
Coláiste na hOllscoile Corcaigh

Deep-Learning-Assisted Robust Detection Techniques for a Chipless RFID Sensor Tag

Nadeem Rather¹, *Student Member, IEEE*, Roy B. V. B. Simorangkir², *Member, IEEE*,
John L. Buckley³, *Member, IEEE*, Brendan O'Flynn⁴, *Senior Member, IEEE*,
and Salvatore Tedesco⁵, *Member, IEEE*

Abstract—In this article, we present a new approach for robust reading of identification (ID) and sensor data from chipless radio frequency ID (CRFID) sensor tags. For the first time, machine-learning (ML) and deep-learning (DL) regression modeling techniques are applied to a dataset of measured radar cross section (RCS) data that have been derived from large-scale robotic measurements of custom-designed, 3-bit CRFID sensor tags. The robotic system is implemented using the first-of-its-kind automated data acquisition method using an ur16e industry-standard robot. A dataset of 9600 electromagnetic (EM) RCS signatures collected using the automated system is used to train and validate four ML models and four 1-D convolutional neural network (1-D CNN) architectures. For the first time, we report an end-to-end design and implementation methodology for robust detection of ID and sensing data using ML/DL models. Also, we report, for the first time, the effect of varying tag surface shapes, tilt angles, and read ranges that were incorporated into the training of models for robust detection of ID and sensing values. The results show that all the models were able to generalize well on the given data. However, the 1-D CNN models outperformed the conventional ML models in the detection of ID and sensing values. The best 1-D CNN model architectures performed well with a low root-mean-square error (RMSE) of 0.061 (0.87%) for tag ID and 0.0241 (3.44%) error for capacitive sensing.

Index Terms—Chipless radio frequency identification (CRFID), convolutional neural networks (CNN), deep learning (DL), electromagnetics (EMs), machine learning (ML), radar cross section (RCS), radio frequency identification (RFID), robots.

I. INTRODUCTION

CONVENTIONAL passive radio frequency identification (RFID) systems have seen widespread adoption in var-

Manuscript received 2 August 2023; revised 3 October 2023; accepted 25 October 2023. Date of publication 28 November 2023; date of current version 29 December 2023. This work was supported in part by the Science Foundation Ireland (SFI) as part of the SFI Centre VistaMilk under Grant SFI 16/RC/3835, in part by the CONNECT Centre for Future Networks and Communications under Grant 13/RC/2077, in part by the Insight Centre for Data Analytics under Grant SFI/12/RC/2289 and Grant 16/RC/3918-CONFIRM, in part by the Enterprise Ireland funded Holistics Disruptive Technologies Innovation Fund (DTIF) under Grant EI-DT20180291-A, and in part by the European Regional Development Fund. The Associate Editor coordinating the review process was Dr. Yang Song. (*Corresponding author: Nadeem Rather.*)

Nadeem Rather, John L. Buckley, Brendan O'Flynn, and Salvatore Tedesco are with the Wireless Sensor Network Group, Tyndall National Institute, University College Cork, Cork, T12R5CP Ireland (e-mail: nadeem.rather@tyndall.ie).

Roy B. V. B. Simorangkir is with the Department of Engineering, Durham University, DH1 3LE Durham, U.K.

Digital Object Identifier 10.1109/TIM.2023.3334378

ious industries, revolutionizing supply chain management, contact-less payments, asset tracking, authentication, animal identification (ID), and sensing for various Internet-of-Things (IoT) applications [1], [2], [3], [4], [5], [6], [7]. However, recent advances have paved the way for chipless RFID (CRFID), which eliminates the need for an integrated circuit silicon device component and offers cost-effectiveness, flexibility, sensing capabilities, as well as enhanced security [8], [9], [10], [11], [12]. In CRFID systems, frequency-domain (FD) and time-domain (TD) approaches are the two main techniques used for encoding and decoding information without the use of a silicon integrated circuit component.

In the FD technique, the information is encoded by manipulating the resonant frequencies or spectral characteristics of a tag antenna. The reader device transmits an electromagnetic (EM) wave and analyzes the frequency response of the tag using the backscattered EM wave to extract the encoded information. On the other hand, in TD approaches, the focus is on the examination of the temporal characteristics of the tag. Information encoding is accomplished by modulating the time delay or phase shift of the tag's response to the interrogating signal from the reader [10], [13].

The FD techniques, particularly using radar cross section (RCS), have been extensively explored due to their low design complexity for the development of CRFID tags [10], [12]. RCS-based CRFID tags encode data by modifying the reflective pattern of the tag antenna through variations of the antenna's shape, size, or material properties. The encoded data can be retrieved from the scattered EM fields that the reader receives.

In the literature, the predominant emphasis has been on advancing CRFID tag performance than on reader implementation due to the complexity of adapting to various tag designs and encoding methods, resulting in a lack of standardized CRFID detection techniques. Conventional signal processing methods, including short-time Fourier transform (STFT) [14], wavelet-based techniques [15], [16], threshold-based detection [17], moving average with threshold detection [18], and signal space representation (SSR) [19], have been explored to identify the data from EM signatures in CRFID systems.

However, these approaches face challenges to consistently provide reliable results across diverse tag designs and sensing configurations, necessitating specific hardware configurations, antenna designs, or signal processing algorithms for accurate detection. For instance, both STFT and wavelet-based

techniques encounter challenges when analyzing signals from high-capacity RFID tags. These challenges include addressing the tradeoff between time and frequency resolution, which can lead to inaccuracies in frequency characterization, as well as handling nonstationary signal behavior and adapting to the dynamic characteristics of high-data-capacity tags [20], [21]. Furthermore, the SSR technique, which aims to determine the minimum distance between received frequency signature points and fixed reference points, also grapples with issues related to adaptability and robustness [22], [23]. This specificity can make deploying CRFID systems in various applications and environments challenging without extensive customization and optimization efforts.

To reduce the reading complexity, several studies have leveraged the pattern recognition capabilities of both machine learning (ML) and its subfield, deep learning (DL), to effectively detect different EM signatures and retrieve accurate tag information [22], [24], [25], [26], [27].

Compared to the conventional signal processing methods mentioned above, the ML/DL approach offers a more flexible and adaptable solution for CRFID systems. By leveraging ML/DL algorithms and models, the CRFID systems can be designed to learn and adapt to different encoding techniques without the need for explicit rule-based programming or hardware modifications. The ML/DL algorithms can analyze the complex patterns and relationships within the CRFID data and extract meaningful information. These algorithms can also handle variations in signal strength, noise, and interference, leading to improved detection and ID accuracy.

Hajizadegan and Chen [24] used an RCS-based CRFID tag for hand gesture recognition. The tag is developed using three split-ring resonators to create a specific 3-bit EM signature in the backscattered EM wave. A feedforward artificial neural network (ANN) is utilized for training the models and for successfully classifying the eight possible combinations. Khadka et al. [22] utilized a DL-based security model to provide a high accuracy of greater than 93% when classifying a cloned tag from a genuine CRFID tag, even in the presence of additive RF interference in real time. Villa-Gonzalez et al. [25] used RCS-based tags to develop a segregation system for a plastic recycling application. A random forest (RF) classifier is trained with a dataset consisting of 300 data points to identify two plastic types (two IDs). The authors achieved an accuracy of 90% when classifying the two plastic types from homogenous bales. In another scenario involving nonhomogeneous bales, an accuracy of 65% was attained. Sokoudjou et al. [26] proposed a comprehensive workflow for ID applications using ML. Three datasets are utilized for the implementation of ML models. When classifying a 4-bit CRFID tag, two datasets consisting of 2400 instances with 600 measurements per tag and 5600 instances with 900 measurements per tag are utilized to achieve a 100% accuracy rate. These studies have achieved impressive results in classifying CRFID tags based on their EM signatures and RCS properties.

However, there are some important gaps in the existing literature that need to be addressed. Specifically, the impact of varying surface shapes on CRFID tag detection has not been

extensively investigated, despite its relevance to real-world applications (such as supply chain management, asset tracking, healthcare, and medical environments, where varying surface shapes can be encountered). In consideration of real-world applications, simultaneous extraction of tag ID and sensing information from CRFID tags using ML approaches has not been explored either. In addition, the focus on classification tasks leaves a gap in the exploration of regression-based approaches for precise and continuous prediction of tag ID and sensing information. Classification tasks identify the presence or absence of specific attributes in CRFID tags. However, it lacks the necessary granularity for certain real-world applications. For example, in supply chain management, merely knowing if a CRFID-tagged perishable item is “Within Required Temperature” or “Out of Required Temperature” is inadequate. Precise predictions of attributes, such as temperature and humidity, are thus crucial for ensuring quality in such scenarios. In an effort to address the aforementioned gaps, this article investigates the following:

- 1) the impacts of varying tag surface shapes, orientations, and read ranges for the development of robust detection algorithms suitable for real-world implementation, aligning with the primary objective of incorporating ML/DL techniques in CRFID systems;
- 2) the feasibility of extracting both ID and sensing information from EM signatures;
- 3) the use of regression-based approaches for accurate and continuous prediction of tag IDs and sensing values;
- 4) the utilization of a comprehensive dataset acquired through an automated data acquisition system, distinguishing it from prior studies.

Through these investigations, this article contributes to a more comprehensive understanding and practical implementation of ML/DL-assisted CRFID systems. This article is structured as follows. In Section II, we provide the intricate details of the CRFID sensor tag design, the instrumentation setup, RCS measurements, and the systematic automated data acquisition methodology. Section III is dedicated to a comprehensive study of ML- and DL-based modeling techniques. Moving forward to Section IV, we present the results obtained from these models, highlighting the best-performing techniques that are validated through a real-world demonstration. In Section V, we analyze the implications of our findings, compare them with previous research, and examine potential future improvements and research directions. Finally, in Section VI, we conclude this article and discuss conceivable directions for future work.

II. RESEARCH METHODOLOGY

A single-layer 3-bit capacity RCS-based CRFID sensor tag was developed based on the design methodology discussed in [9]. There are eight possible ID combinations with three sensing states associated with each ID. This results in a total of 24 sensing tags that need to be characterized. Furthermore, a first-of-its-kind automated data acquisition method using a robot was developed and utilized to obtain the dataset for ML/DL implementation.

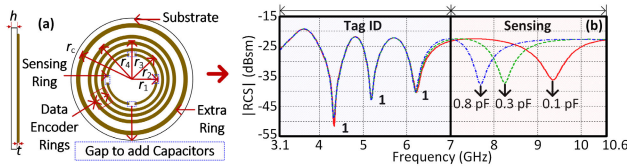


Fig. 1. 3-bit CRFID sensor tag. (a) Topology (dimensions in millimeters are: $r_1 = 6$, $r_2 = 7.12$, $r_3 = 8.45$, $r_4 = 10.03$, $r_c = 14.13$, $h = 0.125$, and $t = 0.01$). (b) Simulated EM RCS response of tag ID 7 with 0.1-, 0.3-, and 0.8-pF sensing points.

A. 3-Bit CRFID Sensor Tag

A 3-bit polarization-insensitive capacitive sensing RCS-based CRFID tag is developed using nested circular ring resonators. The tag is fabricated through a screen printing process with a polyester mesh screen (300M) of an elastic silver ink WIK21285-89A from Henkel (conductivity = 3.94×10^6 S/m) on a flexible polyethylene terephthalate (PET) substrate ($\epsilon_r = 2.9$ and $\tan \delta = 0.0025$). The printed tag was sintered in an oven at 120° for 15 min. The tag consists of an outermost ring to enable the null encoding, an innermost ring for sensing, and three rings in between for 3-bit ID data encoding (Fig. 1). The procedure of tag design is described in [9], and optimized dimensions are provided in the caption of Fig. 1. For the sensing feature, materials with stimuli-sensitive permittivity are to be added to the innermost ring, altering the ring's resonance position upon exposure to appropriate stimuli (e.g., humidity, temperature, and light, to name a few) [12], [28]. For simplicity, this mechanism is demonstrated in this work by simply adding capacitors with varying capacitance values.

The tag is designed so that both the encoded ID and sensing information are carried within the ultrawideband (UWB) frequency of 3.1–10.6 GHz. The data encoding of the tag ID [ranging from “000” (ID 0) to “111” (ID 7)] is encoded within the frequency range of 3.1–7 GHz, while the remaining frequencies of 7–10.6 GHz are used to encode the sensing information. For each tag ID, three capacitance values of 0.1, 0.3, and 0.8 pF are used, demonstrating three sensing states.

An example of the tag's RCS response is shown in Fig. 1(b), showing the case of tag “111” (ID 7) with three capacitance values. The example illustrates that, in this work, the variation in amplitude is utilized for detecting different IDs, while the frequency shift indicates the sensing information.

B. Experimental Setup and Data Collection Methodology

For the purpose of collecting data for this investigation, the system shown in Fig. 2 was developed. All 24 possible tag combinations were evaluated. For each combination, data were collected for tags measured from four different positions (P_1 – P_4) and five distinct mounting platforms (i.e., cases C_1 – C_5). P_1 and P_3 correspond to the two read ranges (200 and 300 mm), while P_2 and P_4 correspond to the 45° tilt at these two read ranges. The variation of the mounting platform reflects five variations in the tag's physical deformation. This was facilitated by a customized polystyrene foam structure [see Fig. 2(c)]. The flat side of the structure was utilized for the case of the tag mounted on a flat surface (C_1). The edges of

the same side were utilized for the cases of the tag corner bent with a length ratio of 50:50 (C_{ii}) and 25:75 (C_{iii}). In addition, the structure includes two round surfaces with radii of 40 and 10 mm. These surfaces were used for the cases of the tag cylindrically bent (C_{iv} and C_v).

1) *Instrumentation Setup*: Furthermore, to obtain the RCS of the tags, the setup shown in Fig. 2(a) was utilized, consisting of an Anritsu MS2038C vector network analyzer (VNA) interfaced with a Raspberry Pi (RPI) module using a Secure Shell (SSH) interface and the programming language Python. Libraries, such as PyVISA, NumPy, and Pandas, were utilized for communication and computations. Port 1 of the VNA was connected to a Schwarzbeck BBHA 9120 D—double-ridged broadband horn antenna for transmitting and receiving EM waves [29]. The VNA was used to generate a frequency sweep from 3.1 to 10.6 GHz with 0-dBm RF output power and to record the input reflection coefficient (S_{11}) at Port 1. The VNA has an average noise floor of -76 dBm from 3.1 to 10.6 GHz, and 700 sampling points were specified for the measurement. The speed of data acquisition was primarily determined by the intermediate frequency bandwidth (IFBW) of the VNA, which, in our case, was set to 10 kHz. These measurement settings resulted in a sweep time of approximately 1 s for each data acquisition. With the specified noise floor, an approximated SNR of 26 dB was obtained across all investigated cases with the tag-to-receiver distance of 300 mm. As the distance is increased, the SNR will decrease and the tag will eventually be unreadable (i.e., when the tag-to-receiver distance is approximately 600 mm).

2) *RCS Calculation*: To obtain the RCS response of the tag from the measured S_{11} , the calibration method derived from [30] was used. Once secure communication between the VNA and Rpi was established, the S -parameter (.S2P) files were acquired from the VNA. The monostatic RCS was calculated using the open-source Python package Scikit-RF, following the formula:

$$\text{RCS}(\sigma) = \left| \frac{(S_{11\text{Tag}} - S_{11\text{Iso}})}{(S_{11\text{Ref}} - S_{11\text{Iso}})} \right|^2 \times \sigma_{\text{ref}}(\lambda) \text{ m}^2 \quad (1)$$

where $S_{11\text{Tag}}$, $S_{11\text{Iso}}$, and $S_{11\text{Ref}}$ represent the scattering parameters of the tag, isolation, and reference, respectively. The known RCS of the reference flat metal plate for calibration [$\sigma_{\text{ref}}(\lambda)$] was calculated using the following equation:

$$\sigma_{\text{ref}}(\lambda) = \frac{4\pi A^2}{\lambda^2}, \quad \text{m}^2 \quad (2)$$

where A is the area of the plate and λ is the wavelength.

3) *Robot-Based Automated Data Collection*: The flow of the data acquisition is explained as follows. First, the 24 tags were each manually mounted on the same side of the 24 foams (e.g., C_i). The pick-and-place process of the foams (with mounted tags) was automated using the Universal Robot (UR16e), which has six rotating joints, a maximum move speed of 120° – 180° per second, and a repeatability tolerance of ± 0.05 mm. The UR16e robot was programmed using Universal Robot Script (URScript), a language specific to Universal Robots, following the flowchart shown in Fig. 3. Initially, the robot is at the rest/wait position, and a measurement with all the structures in place with the exception of the tag was

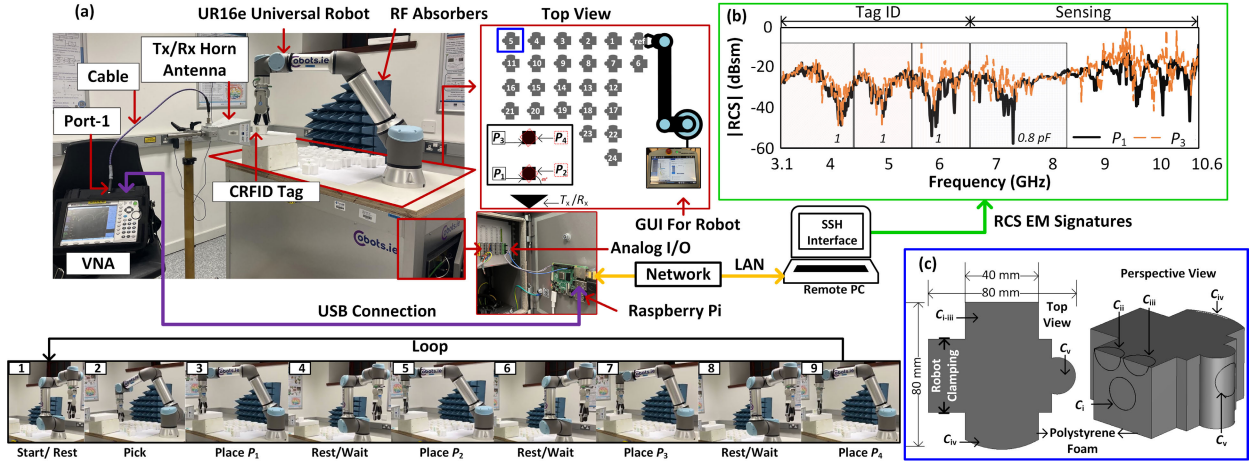


Fig. 2. (a) Automated RCS data acquisition setup. (b) Measured RCS of tag ID 7 with 0.8-pF sensing value at P_1 and P_3 . (c) Polystyrene-made platform for mounting the tag under investigation.

undertaken to record $S_{11_{\text{Iso}}}$. Furthermore, the robot receives a movement signal to pick and place the foam structure with the reference calibration plate (attached to its flat side). A square flat copper plate (25×25 mm) was utilized for calibration purposes. The robot arm then returns to the rest/wait position, and measurement $S_{11_{\text{Ref}}}$ is taken. The robot is then instructed with a second movement signal to return the foam with the reference plate to its original position, followed by the pick, place (P_1 – P_4), record $S_{11_{\text{Tag}}}$, and return of tags #1–#24. The first two calibration steps ($S_{11_{\text{Iso}}}$ and $S_{11_{\text{Ref}}}$) were performed once, followed by the RCS calculations of all 24 tags. Further details on the process are available in [31]. Upon the completion of C_i , the tags were manually mounted to different sides of the foam, and the same process was repeated. For each measurement scenario, 20 readings were recorded to account for varying noise levels and interferences. This yields a total dataset of 9600 EM signatures (i.e., 24 tags \times 4 positions \times 5 shapes \times 20 readings). In Fig. 2(b), a representative example of the collected measured signatures is shown for tag ID 7, with a capacitance value of 0.8 pF measured at positions P_1 and P_3 , displaying different levels of noise.

III. ML AND DL MODELING

Supervised ML/DL involves training models using labeled datasets to make predictions or classifications based on the provided labels. For our dataset, which requires the prediction of numerical values from given inputs instead of classes, we employ regression models. We assess the performance and suitability of four popular ML regression models: support vector regression (SVR), decision trees (DTs), gradient boosted trees (GBT), and RF. In addition, we also explore the application of DL architectures, focusing in particular on the use of 1-D convolutional neural networks (1-D CNNs) in a regression-based approach. One-dimensional CNNs offer a potent approach for extracting intricate patterns and relationships from complex time-series datasets. By incorporating a 1-D CNN into our analysis, we aim to take advantage of its ability to capture relevant features and enhance the predictive capabilities of our models.

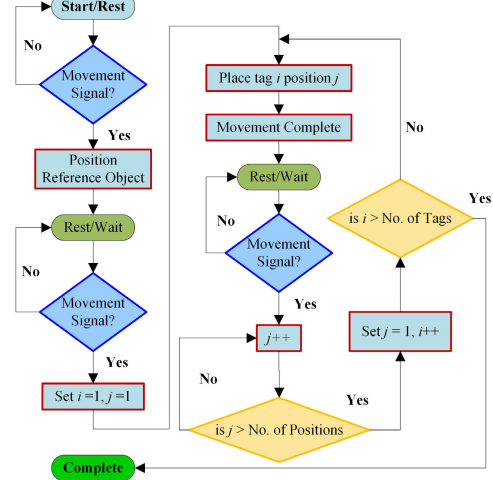


Fig. 3. Robot's operation flow during the pick-and-place of platform-mounted tags.

A. ML-Based Models

Once the dataset was acquired, a series of preprocessing steps was applied to the raw dataset in order to implement the ML models. The flow of the procedure used to implement ML models is shown in Fig. 4. Initially, the raw RCS signatures were low-pass filtered using a fourth-order Butterworth filter with a cutoff frequency of 0.1 Hz, effectively reducing noise while retaining RCS EM signatures used for encoding. This was performed to smoothen the EM signatures and reduce unwanted noise in the signal. In addition, the appropriate output labels were added to the dataset. In regression-based ML, extracting relevant features from the raw dataset is a critical step for attaining accurate predictions.

To streamline this process, a Time Series Feature Extraction Library (TSFEL) was employed to extract a wide range of informative features from the given EM signatures [32]. By utilizing TSFEL, the feature extraction task becomes more efficient and comprehensive. It offers a collection of built-in algorithms for capturing the essential characteristics of 1-D data, including statistical measures, signal processing

techniques, and information theory-based features. A total of 780 features were automatically extracted using this method. These features were acquired from the full frequency band ranging from 3.1 to 10.6 GHz, which covered a total of 700 data samples of the EM signatures. Furthermore, we included manually extracted features from specific frequency bands where relevant minima were to be found, along with their respective RCS magnitude values. We divided the data into four windows: the first window spanned from 3.1 to 4.2 GHz, the second window spanned from 4.2 to 5.2 GHz, and the third window spanned from 5.2 to 6.3 GHz. These windows were utilized to capture crucial information related to the detection of ID minima. The fourth window covered the frequency range from 6.3 to 10.6 GHz and was focused on extracting features associated with sensing information. Utilizing these methods, a total of 788 features were extracted.

After filtering and feature extraction, the dataset was split into training, validation, and test sets. The split was stratified to ensure that the distribution of labels across the different cases remained balanced within all subsets. The data were initially split into a test set, which comprised 20% of the original data, with the remaining 80% of the data further divided into training and validation sets with a split ratio of 75:25. A normalization method, specifically the “StandardScaler” from the scikit-learn library, was then applied to the training dataset. The mean and standard deviation obtained from the training set were then used to transform the validation and test sets. For the ML model implementation, we employed a comprehensive pipeline approach to train and compare the aforementioned regression models. The pipeline encompassed several key steps.

First, we applied feature selection using recursive feature elimination with cross validation (RFE-CV) for each regression model. RFE-CV performed iterative feature elimination based on their impact on the model’s performance, while cross validation was utilized to ensure the robustness of the feature selection process. Following feature selection, we conducted hyperparameter optimization using GridSearchCV. The list of hyperparameters examined for optimization is available in Fig. 4. The models were fine-tuned for best performance and generalization using hyperparameter optimization. Following our investigations in [33], each ML model was implemented for ID and sensing (capacitance values in picofarads) predictions separately.

Each model was first trained using the training set (X_{train} , y_{train}), and subsequently, predictions were made on the validation set (X_{val} , y_{val}) to ensure no overfitting. If no overfitting was detected, the defined model was set and trained on the combined (X_{dev} , y_{dev}) training and validation sets (80%) and then evaluated on the 20% test data (X_{test} , y_{test}). The root-mean-square error (RMSE) was utilized as an evaluation metric to quantify the prediction performance of each regression model. By employing this detailed pipeline approach, we aimed to compare the performance of the four regression models in terms of their ability to accurately predict the ID and sensed capacitance value of the target tag. The goal

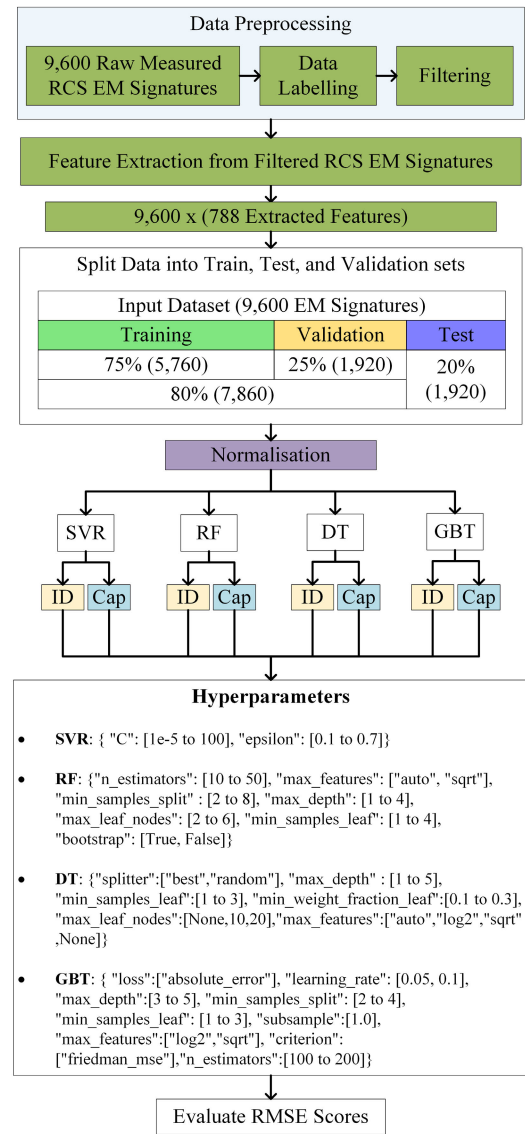


Fig. 4. ML implementation process flow with hyperparameters.

was to identify the best-performing model and capitalize on its strengths to increase prediction accuracy and generalization capability in the given task.

B. DL Architectures

To explore the potential of DL models, we implemented four distinct 1-D CNN architectures, each tailored for ID and capacitance value prediction. These architectures use 1-D CNNs to extract meaningful features from the input data and make accurate predictions. These architectures were implemented using the Keras library with TensorFlow as the backend. The model architectures consisted of multiple layers, including convolutional layers (Conv1D), pooling layers, dropout layers, batch normalization layers, and dense layers. DL models are built to automatically learn and extract hierarchical representations of the input data during the training process. As a result, the model can learn and extract features directly from the raw data. The filtered signals were thus

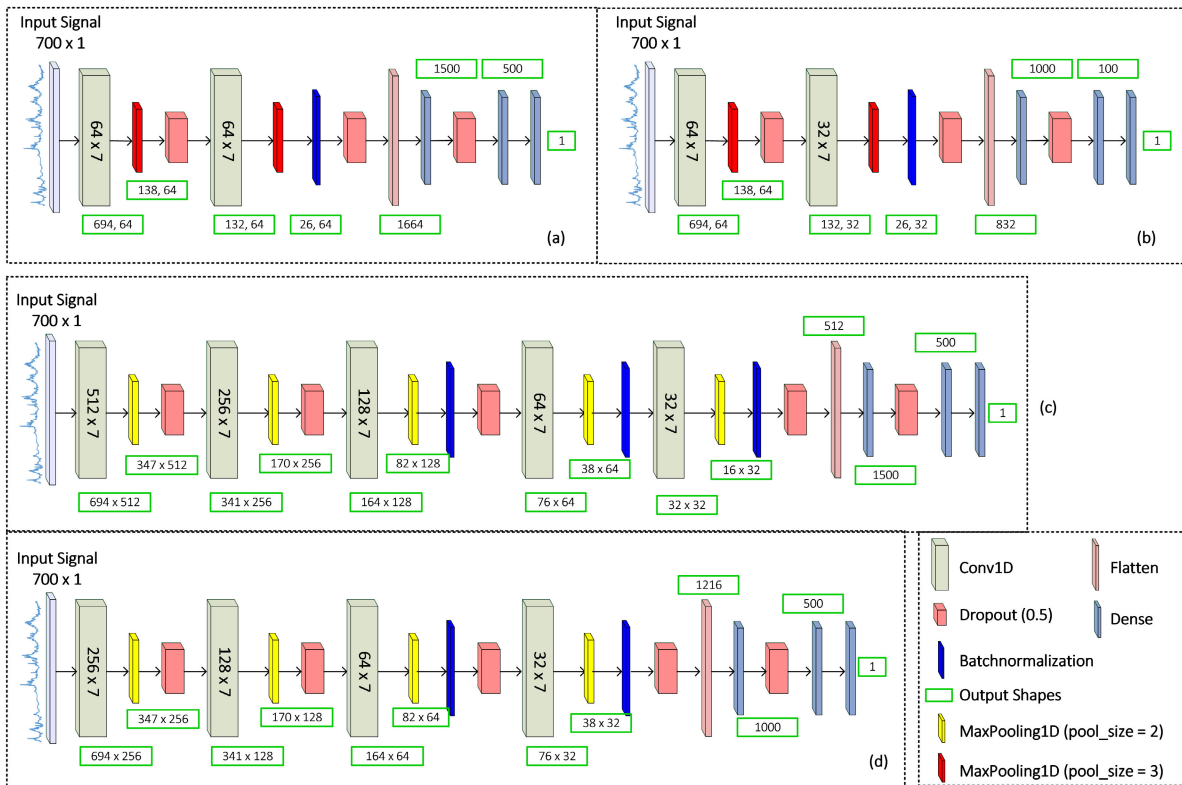


Fig. 5. 1-D CNN architectures. (a) Model 1 for Tag ID. (b) Model 2 for sensing. (c) Model 3 for Tag ID. (d) Model 4 for sensing.

used as the input to these models. The split and normalization procedure was kept similar to the ML models (see Fig. 4).

1) *Model 1—Tag ID*: The first model [Fig. 5(a)] is intended for tag ID prediction. It consists of several layers, starting with the EM signature as the input layer. The input layer considers the data's feature dimensions, which are (700, 1), signifying 700 data points with a single feature. This is followed by a Conv1D layer with 64 filters and a kernel size of 7, which helps capture local patterns in the input data. A MaxPooling1D layer is then applied to reduce the spatial dimensions of the data. To prevent overfitting, a dropout layer with a rate of 0.5 is included. Another Conv1D layer with 64 filters and a kernel size of 7 follows, further extracting relevant features. This is again followed by a MaxPooling1D layer and a BatchNormalization layer for normalization. Dropout is applied once more before flattening the output. The flattened data are then passed through fully connected layers with rectified linear unit (ReLU) activation functions, consisting of a dense layer with 1500 units, a dropout layer with a rate of 0.5, and a dense layer with 500 units. Finally, a dense layer with a linear activation function is used in the output layer for regression-based tag ID prediction.

2) *Model 2—Tag Sensing*: The second model focuses on the tag capacitance value prediction [Fig. 5(b)]. Similar to the first model, it starts with an input layer and then proceeds with a Conv1D layer with 64 filters and a kernel size of 7. This is followed by a MaxPooling1D layer for downsampling and a dropout layer for regularization. Another Conv1D layer with 32 filters and a kernel size of 7 is applied, followed by another MaxPooling1D layer and a BatchNormalization layer. Dropout

is included to further prevent overfitting. The output is then flattened and passed through fully connected layers, consisting of a dense layer with 1000 units, a dropout layer with a rate of 0.5, and a dense layer with 100 units. The output layer uses a linear activation function for regression-based capacitance values prediction.

3) *Model 3—Tag ID (Extended)*: The third model is an extended version of the tag ID prediction Model 1. It includes additional Conv1D layers to capture more complex patterns [Fig. 5(c)]. The architecture starts with an input layer and proceeds with a Conv1D layer with 512 filters and a kernel size of 7. A MaxPooling1D layer is then applied for downsampling, followed by dropout for regularization. The subsequent layers consist of Conv1D layers with 256, 128, 64, and 32 filters, accompanied by a MaxPooling1D layer, BatchNormalization layer, and dropout layer. The output is flattened and passed through fully connected layers, including a dense layer with 1500 units, a dropout layer, a dense layer with 500 units, and a final dense layer with a linear activation function for tag ID prediction.

4) *Model 4—Tag Sensing (Extended)*: The fourth model is an extended version of the tag capacitance value prediction Model 2. It incorporates additional Conv1D layers to capture more intricate patterns in the data [Fig. 5(d)]. The architecture starts with an input layer, followed by Conv1D layers with 256, 128, 64, and 32 filters, each accompanied by a MaxPooling1D layer, BatchNormalization layer, dropout layer, and MaxPooling1D layer. The flattened output is then passed through fully connected layers, consisting of a dense layer with 1000 units, a dropout layer, a dense layer with 500 units,

TABLE I
SUMMARY OF RMSE RESULTS

Model	Tag ID 0-7			Sensing (0.1 pF - 0.8 pF)		
	Train	Val*	Test	Train	Val*	Test
SVR	0.612	0.616	0.600	0.226	0.233	0.227
GBT	0.249	0.315	0.300	0.114	0.137	0.127
DT	1.122	1.114	1.076	0.271	0.273	0.269
RF	0.906	0.889	0.916	0.260	0.261	0.259
1D CNN-1,2	0.108	0.086	0.098	0.026	0.031	0.0304
1D CNN-3,4	0.073	0.084	0.061	0.019	0.030	0.0241

Best performing model is highlighted in bold (Val = Validation)*

and a final dense layer with a linear activation function for capacitance prediction. No padding was used in any layer of the architecture.

All the discussed architectures were trained using the Adam optimizer with the mean squared error (mse) loss function. The training process involved a batch size of 32 and was conducted over 300 epochs. Early stopping was implemented to monitor the training process and halt if the loss did not improve for a certain number of epochs. Model checkpoints were saved to retain the best-performing model. The training loss was tracked to assess the convergence and overall performance of the models. The evaluation of the trained models was performed using the RMSE as the evaluation metric, measuring the average deviation between the predicted and actual values. Similar to the ML model implementation, the models were trained first on the training set, followed by a validation set to make sure that there was no overfitting. Finally, if no overfitting was detected, the architectures were trained on the development set and tested on the unseen test dataset.

IV. RESULTS

A summary of RMSE results from the ML and DL models is shown in Table I. For all investigated models, the evaluation results on the training, validation, and test sets are given. It is seen that both ML models and 1-D CNN architectures were able to generalize well with the data to make predictions on ID and capacitance values. As shown, the GBT model achieved the best performance with an RMSE of 0.3 (normalized RMSE: 4.2%) on the test set for tag ID prediction, while its sensing prediction RMSE was relatively high with 0.127 (18.4%). SVR performed slightly better compared to the DT and RF in detecting both ID and capacitance values. However, all these models had a significantly high RMSE for the capacitance value prediction. Moving on to the DL architectures, for tag ID prediction, 1-D CNN Model 1 achieved a low RMSE of 0.098 (1.2%) on the test set. In terms of sensing prediction, the RMSE was 0.0304 (4.3%). These are significantly better than the best-performing GBT model, with a 67.33% and 73.23% decrease in RMSE error for tag ID and sensing values, respectively.

The deeper 1-D CNN architectures (Models 3 and 4) achieved even better results with an RMSE of 0.061 (0.87%) and 0.0241 (3.44%) for ID and sensing, respectively.

Compared to 1-D CNN Models 1 and 2, the RMSE was reduced by 37.76% and 20.78%, respectively. In summary,

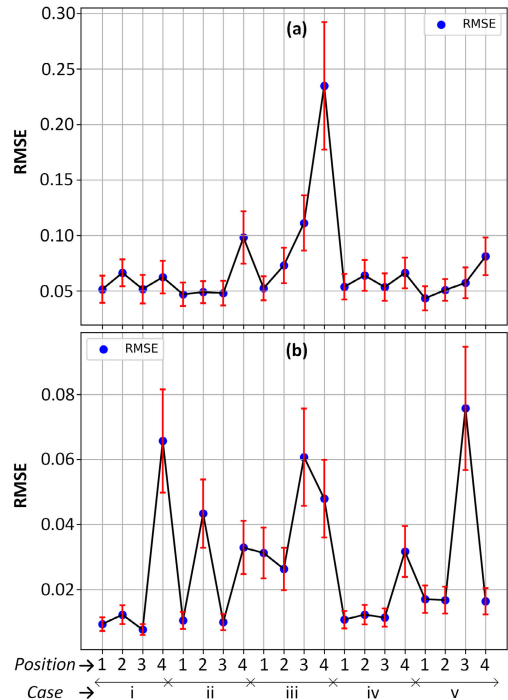


Fig. 6. RMSE and standard deviation results from different tag positions (i.e., P_1-P_4) and tag deformations (i.e., C_1-C_v) for (a) tag ID using Model 1 and (b) sensing using Model 2.

among the ML models, GBT exhibited the lowest RMSE for both tag ID and capacitance value prediction tasks. On the other hand, the 1-D CNN architectures remarkably outperformed the ML models. These findings suggest that DL approaches using 1-D CNN have the potential to provide valuable insights and accurate predictions in this domain compared to classical ML models based on feature extraction.

For a more detailed analysis of the achieved results, the four 1-D CNN models are further evaluated for all 20 cases (i.e., four positions \times five shapes). The RMSE for tag ID and capacitance value prediction at different cases and positions as obtained from Models 1 and 2, respectively, is shown in Fig. 6. It is seen that the RMSE of Model 1 is consistent for all cases except for C_{iii} , at the longer read range with 45° tilt (P_4) scenario. Similarly, for capacitance sensing value, the prediction shows that the RMSE is slightly higher at the P_4 positions. Furthermore, in Models 3 and 4, the RMSE shows similar trends (as shown in Fig. 7) with slightly more consistent and lower values of RMSE. The capacitance sensing Model 4 also shows a reduction in RMSE for all cases.

Models 3 and 4 were the best-performing models that were saved to then make predictions in a real-world scenario. To validate the effectiveness of these models, we conducted experiments with an Anritsu MS2038C VNA connected to a horn antenna [29] and interfaced with an RPi. The raw data obtained from the VNA were processed using a custom-written program that employed the RCS computation and the trained Models 3 and 4 for tag ID and capacitance value predictions, respectively. The inference time for model prediction was 1.2 s, resulting in a total time of 2.2 s to capture, process, and make predictions on raw data. Ten (2%) of the total 480 possi-

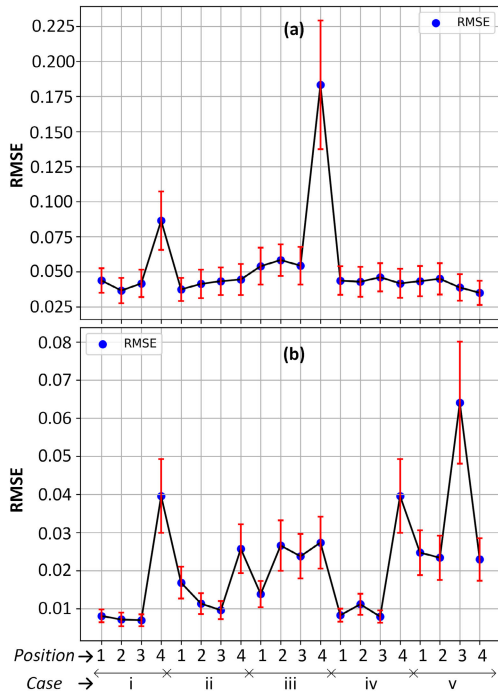


Fig. 7. RMSE and standard deviation results from different tag positions (i.e., P_1 – P_4) and tag deformations (i.e., C_1 – C_v) for (a) tag ID using Model 3 and (b) sensing using Model 4.

ble scenarios ($24 \text{ tags} \times 4 \text{ positions} \times 5 \text{ cases}$) were selected at random and utilized for the validation. As shown in Table II, it is observed that predictions made for ID and capacitance sensing values were generally accurate for different testing scenarios. In practical scenarios, the predicted ID from the regression model would be rounded to the nearest integer. For instance, an ID predicted as 2.7 would be regarded as 3. By employing this rounding method, Table II demonstrates that the ID was predicted correctly in every instance. Similarly, rounding the capacitance values to the nearest value (0.1, 0.3, or 0.8 pF) resulted in accurate capacitance sensing value predictions in eight out of ten instances. The remaining two errors were due to the proximity between the rounded values of 0.1 and 0.3. The variability in errors can also be attributed to the variation in the model’s RMSE for different shapes and positions. The measurement process and an example of the tag ID and capacitance sensing value detection using the trained models are available in a demonstration video, which can be viewed in [34].

V. DISCUSSION

The presented study provides a comprehensive analysis of ML and DL models for tag ID and sensing prediction in CRFID systems. The results demonstrate the effectiveness of both ML and DL approaches, with DL models exhibiting superior performance in terms of accurately predicting tag ID and sensed capacitance values. The findings highlight the potential of DL models, particularly 1-D CNN architectures, in providing valuable insights and accurate predictions in the CRFID domain compared to classical ML models based on feature extraction. The utilization of the dataset acquired

TABLE II
ACTUAL VERSUS PREDICTED VALUES WITH ERRORS

C_{i-v} (P_{1-4})	$ID_{act.}$	$S_{act.}$	$ID_{pred.}$ (Error)	$S_{pred.}$ (Error)
ii (P_2)	3	0.8	2.8981 (0.1019)	0.7360 (0.0640)
v (P_1)	7	0.3	6.9721 (0.0279)	0.2967 (0.0033)
i (P_4)	5	0.3	4.9641 (0.0359)	0.2640 (0.0360)
iii (P_3)	1	0.1	1.0199 (0.0199)	0.1647 (0.0647)
iv (P_1)	2	0.8	2.0138 (0.0138)	0.7599 (0.0401)
i (P_2)	5	0.3	4.8707 (0.2293)	0.3138 (0.0138)
v (P_3)	6	0.3	6.1629 (0.1629)	0.2733 (0.0267)
iii (P_4)	3	0.1	2.8091 (0.1909)	0.1567 (0.0567)
i (P_2)	2	0.3	2.0148 (0.0148)	0.2959 (0.0041)
iv (P_1)	7	0.3	6.6830 (0.3170)	0.2961 (0.0039)

act. = Actual, *pred.* = Predicted, *S* = Capacitance Value (pF)

through an automated data acquisition system sets this study apart from previous research works, which are limited in their dataset size due to the constraints of data collection procedures [25], [26], [27]. The comprehensive dataset enables the development of robust ML/DL models that can learn and adapt to varying EM signatures that encode data. The automation helps to incorporate varying scenarios for the CRFID tags, improving the robustness and reliability of the proposed models and enhancing their practical applicability. Investigating the impacts of varying tag surface shapes, orientations, and read ranges is paramount for real-world implementation. CRFID tags may encounter different surface shapes and orientations in practical scenarios, and the read ranges may vary. The developed detection algorithms can be optimized by studying these factors to handle diverse environmental conditions and ensure reliable tag detection.

Furthermore, the feasibility of extracting both ID and sensing information from the EM signatures is another significant contribution of this study. Traditionally, CRFID systems have focused primarily on tag ID [25], [26]. However, by exploring the extraction of sensing information from the EM signatures, this research paves the way for leveraging CRFID technology in applications that require continuous monitoring and sensing capabilities (e.g., for food quality monitoring and health monitoring [12]), expanding the potential applications of CRFID systems beyond simple ID tasks. The study also investigates regression-based approaches for accurate and continuous prediction of tag IDs and sensed capacitance values. This regression-based approach enables precise and continuous prediction of tag information, which is particularly useful in applications where real-time and continuous monitoring is crucial. The results obtained from these regression models provide insights into the potential accuracy and reliability of CRFID systems in predicting tag IDs and sensing values. Likewise, with reduced hardware complexity typically associated with conventional signal processing methods, our research aligns with the goal of miniaturizing CRFID systems for improved portability. This advancement holds the potential to enhance the sensitivity of cost-effective readers [35], resulting in more efficient and resilient tag detection [36].

Furthermore, this article aims to highlight one of the possible future impacts of integrating ML/DL with RFID and antenna technology, with other promising applications

being investigated for antenna design optimizations, RF signal processing, and so on in [37], [38], and [39]. While ML/DL has not yet made significant strides in this field, we anticipate that this will change soon, paving the way for advancements in this evolving field and ultimately transforming industries such as supply chain management, logistics, health monitoring, chipless and sustainable Identification, and sensing technologies.

There are, however, certain limitations and challenges that need to be acknowledged. First, the effectiveness of the proposed algorithms and models may be influenced by the specific hardware configurations and antenna designs. The customization and optimization efforts required for different hardware configurations and encoding techniques should be considered for practical implementation.

VI. CONCLUSION

ML and DL models were implemented in this article for a 3-bit CRFID sensor tag. For the first time, an automated data acquisition methodology was utilized to collect a comprehensive dataset to implement these models incorporating varying surface shapes, read ranges, and tilt angles for robust detection. A thorough analysis of four popular ML models, namely, SVR, GBT, DT, and RF, was carried out. Furthermore, 1-D CNN architectures were applied for our analysis as well. It was found that the GBT performed well in the ML models; however, CNN models outperformed all ML models with impressive low RMSE of 0.061 (0.87%) and 0.0241 (3.44%) for ID and sensing, respectively. The 1-D CNN architectures thus display an impressive outcome in generalizing well to the given EM signatures with varying parameters. The best models were used to infer predictions in real-world scenarios with successful results. In future, our goal is to further enhance those models and lower the RMSE in a wide range of cases while also developing models for higher bit capacity tags.

REFERENCES

- [1] K. Finkenzerler, *RFID Handbook: Fundamentals and Applications in Contactless Smart Cards, Radio Frequency Identification and Near-Field Communication*. Hoboken, NJ, USA: Wiley, 2010.
- [2] A. Sarac, N. Absi, and S. Dauzère-Pérès, "A literature review on the impact of RFID technologies on supply chain management," *Int. J. Prod. Econ.*, vol. 128, no. 1, pp. 77–95, Nov. 2010.
- [3] L. Catarinucci, S. Tedesco, and L. Tarricone, "On the use of UHF RFID antenna systems customized for robotic applications," in *Proc. IEEE Int. Symp. Antennas Propag.*, Jul. 2012, pp. 1–2.
- [4] L. Catarinucci, S. Tedesco, D. De Donno, and L. Tarricone, "Platform-robust passive UHF RFID tags: A case-study in robotics," *Prog. Electromagn. Res. C*, vol. 30, pp. 27–39, 2012.
- [5] M. Pigeon, N. Rather, B. O'Flynn, and J. Buckley, "NFC sensing of tear fluid for animal health monitoring," in *Proc. 15th Eur. Conf. Antennas Propag. (EuCAP)*, Mar. 2021, pp. 1–5.
- [6] C. Peres et al., "Theoretical models for underwater RFID and the impact of water salinity on the design of wireless systems," *Int. J. Adv. Netw. Services*, vol. 13, no. 34, pp. 45–59, 2020.
- [7] D. R. Gawade et al., "A battery-less NFC sensor transponder for museum artefact monitoring—A review of NFC sensor technology and a proposed solution," in *Proc. SENSORCOMM*, Nice, France, Oct. 2019.
- [8] E. Perret, *Radio Frequency Identification and Sensors: From RFID to Chipless RFID*. Hoboken, NJ, USA: Wiley, 2014.
- [9] N. Rather, J. Buckley, B. O'Flynn, and M. Pigeon, "A novel RCS based CRFID tag design," in *Proc. 16th Eur. Conf. Antennas Propag. (EuCAP)*, Mar. 2022, pp. 1–5.
- [10] S. Preradovic and N. C. Karmakar, "Chipless RFID: Bar code of the future," *IEEE Microw. Mag.*, vol. 11, no. 7, pp. 87–97, Dec. 2010.
- [11] N. Rather, R. B. V. B. Simorangkir, J. Buckley, and B. O'Flynn, "Flexible and semi-transparent chipless RFID tag based on PDMS-conductive fabric composite," in *Proc. Int. Workshop Antenna Technol. (iWAT)*, May 2022, pp. 33–36.
- [12] N. C. Karmakar, E. M. Amin, and J. K. Saha, *Chipless RFID Sensors*. Hoboken, NJ, USA: Wiley, 2016.
- [13] C. Herrojo, F. Paredes, J. Mata-Contreras, and F. Martín, "Chipless-RFID: A review and recent developments," *Sensors*, vol. 19, no. 15, p. 3385, Aug. 2019.
- [14] Y. Zhang, Z. Guo, W. Wang, S. He, T. Lee, and M. Loew, "A comparison of the wavelet and short-time Fourier transforms for Doppler spectral analysis," *Med. Eng. Phys.*, vol. 25, no. 7, pp. 547–557, Sep. 2003.
- [15] G. Khadka, M. A. Bibile, L. M. Arjomandi, and N. C. Karmakar, "Analysis of artifacts on chipless RFID backscatter tag signals for real world implementation," *IEEE Access*, vol. 7, pp. 66821–66831, 2019.
- [16] A. Lazaro, A. Ramos, D. Girbau, and R. Villarino, "Chipless UWB RFID tag detection using continuous wavelet transform," *IEEE Antennas Wireless Propag. Lett.*, vol. 10, pp. 520–523, 2011.
- [17] C. Divarathne and N. Karmakar, "An advanced tag detection technique for chipless RFID systems," in *Proc. Eur. Microw. Conf. (EuMC)*, Sep. 2015, pp. 251–254.
- [18] R. Koswatta and N. C. Karmakar, "Moving average filtering technique for signal processing in digital section of UWB chipless RFID reader," in *Proc. Asia-Pacific Microw. Conf.*, Dec. 2010, pp. 1304–1307.
- [19] P. Kalansuriya, N. Karmakar, and E. Viterbo, "Signal space representation of chipless RFID tag frequency signatures," in *Proc. IEEE Global Telecommun. Conf. (GLOBECOM)*, Dec. 2011, pp. 1–5.
- [20] R. E. Azim, N. Karmakar, and E. Amin, "Short time Fourier transform (STFT) for collision detection in chipless RFID systems," in *Proc. Int. Symp. Antennas Propag. (ISAP)*, Nov. 2015, pp. 1–4.
- [21] F. Babaeian and N. C. Karmakar, "Time and frequency domains analysis of chipless RFID back-scattered tag reflection," *IoT*, vol. 1, no. 1, pp. 109–127, Sep. 2020.
- [22] G. Khadka, B. Ray, N. C. Karmakar, and J. Choi, "Physical-layer detection and security of printed chipless RFID tag for Internet of Things applications," *IEEE Internet Things J.*, vol. 9, no. 17, pp. 15714–15724, Sep. 2022.
- [23] A. Subrahmannian and S. K. Behera, "Chipless RFID: A unique technology for mankind," *IEEE J. Radio Freq. Identificat.*, vol. 6, pp. 151–163, 2022.
- [24] M. Hajizadegan and P.-Y. Chen, "Gesture recognition using a portable and flexible meta-atom panel and machine learning," in *Proc. IEEE Int. Symp. Antennas Propag. USNC-URSI Radio Sci. Meeting*, Jul. 2019, pp. 637–638.
- [25] F. Villa-Gonzalez, R. Bhattacharyya, and S. Sarma, "Single and bulk identification of plastics in the recycling chain using chipless RFID tags," in *Proc. IEEE Int. Conf. RFID (RFID)*, Apr. 2021, pp. 1–8.
- [26] J. F. Sokoudjou, F. Villa-González, P. García-Cardarelli, J. Díaz, D. Valderas, and I. Ochoa, "Chipless RFID tag implementation and machine-learning workflow for robust identification," *IEEE Trans. Microw. Theory Techn.*, early access, May 25, 2023, doi: 10.1109/TMTT.2023.3276011.
- [27] S. Jeong, M. M. Tentzeris, and S. Kim, "Machine learning approach for wirelessly powered RFID-based backscattering sensor system," *IEEE J. Radio Freq. Identificat.*, vol. 4, no. 3, pp. 186–194, Sep. 2020.
- [28] D. E. Anagnostou, D. Torres, T. S. Teeslink, and N. Sepulveda, "Vanadium dioxide for reconfigurable antennas and microwave devices: Enabling RF reconfigurability through smart materials," *IEEE Antennas Propag. Mag.*, vol. 62, no. 3, pp. 58–73, Jun. 2020.
- [29] *BBHA 9120 D—Double Ridged Broadband Horn Antenna*. Accessed: Oct. 3, 2023. [Online]. Available: <http://www.schwarzbeck.de/en/antennas/broadband-horn-antennas/double-ridged-horn-antenna/404-bbha-9120-d-double-ridged-broadband-horn-antenna.html>
- [30] W. Wiesbeck and D. Kahny, "Single reference, three target calibration and error correction for monostatic, polarimetric free space measurements," *Proc. IEEE*, vol. 79, no. 10, pp. 1551–1558, Oct. 1991.
- [31] N. Rather et al., "A novel robot based data acquisition methodology for chipless RFID systems," in *Proc. IEEE 13th Int. Conf. RFID Technol. Appl. (RFID-TA)*, Sep. 2023, pp. 49–52.
- [32] M. Barandas et al., "TSFEL: Time series feature extraction library," *SoftwareX*, vol. 11, Jan. 2020, Art. no. 100456.

- [33] N. Rather, R. B. V. B. Simorangkir, J. Buckley, B. O'Flynn, and S. Tedesco, "Evaluation of machine learning models for a chipless RFID sensor tag," in *Proc. 17th Eur. Conf. Antennas Propag. (EuCAP)*, Mar. 2023, pp. 1–5.
- [34] N. Rather. (2023). *Demonstration Video of Deep Learning Assisted Chipless RFID Tag Detection*. [Online]. Available: https://youtu.be/cFoC83_jo04
- [35] F. Villa-Gonzalez, J. J. F. Sokoudjou, O. Pedrosa, D. Valderas, and I. Ochoa, "Analysis of machine learning algorithms for USRP-based smart chipless RFID readers," in *Proc. 17th Eur. Conf. Antennas Propag. (EuCAP)*, Mar. 2023, pp. 1–5.
- [36] D. P. Mishra and S. K. Behera, "Resonator based chipless RFID: A frequency domain comprehensive review," *IEEE Trans. Instrum. Meas.*, vol. 72, pp. 1–16, 2023.
- [37] J. Joung, "Machine learning-based antenna selection in wireless communications," *IEEE Commun. Lett.*, vol. 20, no. 11, pp. 2241–2244, Nov. 2016.
- [38] C. Occhiuzzi et al., "Automatic monitoring of fruit ripening rooms by UHF RFID sensor network and machine learning," *IEEE J. Radio Freq. Identificat.*, vol. 6, pp. 649–659, 2022.
- [39] M. A. B. Abbasi et al., "Machine learning-assisted direction-of-arrival accuracy enhancement technique using oversized lens-loaded cavity," *IET Microw., Antennas Propag.*, vol. 16, no. 6, pp. 305–315, May 2022.



Nadeem Rather (Student Member, IEEE) received the bachelor's degree in engineering, specializing in electronics and communication from Visvesvaraya Technological University (VTU), Bengaluru, India, in 2013, and the master's degree in engineering from Christ University, Bengaluru, in 2017, with a focus on communication systems. He is currently pursuing the Ph.D. degree with the Wireless Sensor Networks Group, Tyndall National Institute, University College Cork, Cork, Ireland.

His research focuses on developing advanced artificial intelligence (AI) algorithms and innovative techniques for enhancing the performance and efficiency of radio frequency identification (RFID) systems. His research also encompasses the design of RF antennas tailored for wearable health monitoring applications. In addition, he possesses extensive industry and research experience, enriching his expertise in the field. Throughout his Ph.D. study, his contributions have been recognized through notable accolades.

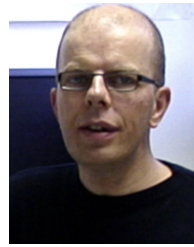
Mr. Rather was honored with the Postgraduate Publication of the Year 2020 Award at the Tyndall National Institute. Furthermore, his research paper secured the First Place in the Best Student Research Paper Category at the International Workshop on Antenna Technology 2021. In addition, his research work was acknowledged with the Best Demonstration Award at the VistaMilk Conference 2023, highlighting the practical impact of his innovative solutions.



Roy B. V. B. Simorangkir (Member, IEEE) received the B.S. degree in telecommunication engineering from the Institut Teknologi Bandung, Bandung, Indonesia, in 2010, the M.S. degree in electrical and electronic engineering from Yonsei University, Seoul, South Korea, in 2014, and the Ph.D. degree in electronic engineering from Macquarie University, Macquarie Park, NSW, Australia, in 2018.

After completing his Ph.D. degree, he pursued post-doctoral research at Macquarie University; the Institute of Electronics and Telecommunications of Rennes, Rennes, France; and the Tyndall National Institute, Cork, Ireland. He is currently an Assistant Professor with the Department of Engineering, Durham University, Durham, U.K., where he specializes in the development of unconventional material-based antennas and sensors for next-generation wireless communication and sensing systems. He has published over 60 refereed research articles in this field, including award-winning work.

Mr. Simorangkir has taken on leadership roles at major international conferences and received recognition as an outstanding reviewer for esteemed journals, notably from 2021 to 2023 for IEEE TRANSACTIONS ON ANTENNAS AND PROPAGATION.



John L. Buckley (Member, IEEE) was born in Cork, Ireland. He received the B.Eng. degree from the Cork Institute of Technology (CIT), Cork, in 1994, and the M.Eng.Sc. and Ph.D. degrees from the Department of Electrical and Electronic Engineering, University College Cork (UCC), Cork, in 2004 and 2016, respectively.

From 1994 to 2002, he was with EMC Corporation, Cork, where he specialized in printed circuit board (PCB) design, high-speed digital design, and signal integrity. He joined the Tyndall National Institute, UCC, in 2005, where he is currently a Senior Researcher and leads the Antenna and RF Team's research activities working on both fundamental and applied antenna and RF research. He has published more than 80 scientific works and acts as a reviewer for several international antenna journals and conferences in the field of antennas and propagation. His research interests include electrically small antenna design, tunable antennas, wearable and implantable antennas, and RF front-end design.

Dr. Buckley served as the General Co-Chair for the International Conference on Antenna Technology (iWAT) in 2022.



Brendan O'Flynn (Senior Member, IEEE) received the B.Eng. (Hons.), M.Eng.Sc., and Ph.D. degrees from University College Cork, Cork, Ireland, in 1993, 1995, and 2016, respectively.

He is currently a Senior Staff Researcher with the Tyndall National Institute, University College Cork, Cork. He is also the Head of the Wireless Sensor Networks (WSN) Group, University College Cork. His research interests include wearable sensing systems, edge-based analytics, sensor system integration, low-power embedded systems design and development, system miniaturization, and RF system design and optimization. He has published widely in these areas and has secured significant funding for the development and deployment of "Smart Sensing" technologies and applied research projects.



Salvatore Tedesco (Member, IEEE) received the B.Sc. degree (Hons.) in information technology engineering and the M.Sc. degree (Hons.) in telecommunications engineering from the University of Salento, Lecce, Italy, in 2008 and 2011, respectively, and the Ph.D. degree in electrical and electronic engineering from University College Cork (UCC), Cork, Ireland, in 2022.

Since April 2012, he has been with the Wireless Sensor Networks Group, Tyndall National Institute, UCC, where he is currently a Senior Researcher and a Team Leader responsible for leading a research team in the wearable and data analytics area. He has authored more than 60 articles in international journals and conference proceedings. He has received over €1.1 million in grant funding as a Principal Investigator and a Co-Principal Investigator. Since joining the Tyndall National Institute, he has managed and successfully led over 20 industrial and research-oriented projects focused on his main research interests on wearable technologies for healthcare and well-being, human motion analysis in sports and clinical populations, digital health, physiological monitoring, signal processing, edge analytics, and machine learning. Further contributions deal with radio frequency identification (RFID) technology and antenna design, ultrawideband localization systems for indoor applications, sensor calibration, and industry 4.0.